



**HAL**  
open science

# A Neural Network Approach for a Fast and Accurate Computation of a Longwave Radiative Budget

F. Chevallier, F. Chéruy, N. Scott, A. Chédin

► **To cite this version:**

F. Chevallier, F. Chéruy, N. Scott, A. Chédin. A Neural Network Approach for a Fast and Accurate Computation of a Longwave Radiative Budget. *Journal of Applied Meteorology*, 1998, 37 (11), pp.1385-1397. 10.1175/1520-0450(1998)0372.0.CO;2 . hal-02946326

**HAL Id: hal-02946326**

**<https://hal.science/hal-02946326>**

Submitted on 30 Apr 2021

**HAL** is a multi-disciplinary open access archive for the deposit and dissemination of scientific research documents, whether they are published or not. The documents may come from teaching and research institutions in France or abroad, or from public or private research centers.

L'archive ouverte pluridisciplinaire **HAL**, est destinée au dépôt et à la diffusion de documents scientifiques de niveau recherche, publiés ou non, émanant des établissements d'enseignement et de recherche français ou étrangers, des laboratoires publics ou privés.



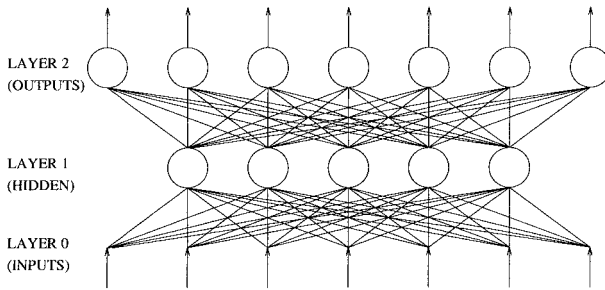


FIG. 1. An example of a single-hidden-layer neural network. The spheres symbolize the neurons.

tive codes are the key to a better account of the diurnal cycle.

Statistical methods draw interesting prospects to solve this contradiction between speed and accuracy. In this paper we present a fast and accurate method for the computation of longwave flux profiles for clear as well as cloudy situations. The scheme, hereafter referred to as “NeuroFlux,” is based on a neural network technique—the multilayer perceptron (MLP), as defined by Rumelhart et al. (1986). The next section is devoted to a brief description of the MLP. In section 3 we review the radiative transfer equations for longwave fluxes in clear and cloudy atmospheres and describe the features of the neural network–based radiative transfer scheme. In section 4 we present the setup of the datasets on which the parameters of the neural networks are inferred. Section 5 presents the results of flux calculations with NeuroFlux.

**2. The multilayer perceptron**

Neural network techniques, among others, allow us to reduce the number of calculations contained in a function  $f: A \rightarrow B$ , where  $A \subset \mathbf{R}^n$  and  $B \subset \mathbf{R}^m$ , by approximating  $f$  with a parameterized function  $g$ :

$$g: A \rightarrow B$$

$$x \rightarrow y = g(\theta, x). \tag{1}$$

The parameters are gathered in vector  $\theta \in \mathbf{R}^p$  and are called “synaptic weights.”

These statistical methods have proved their ability to deal with nonlinear problems, in particular the MLP, as defined by Rumelhart et al. (1986). The MLP relies on processors, called “formal neurons” or “neurons” with reference to the biological analogy. A neuron computes a weighted sum of its inputs and transfers this signal through a sigmoidal function (here the hyperbolic tangent). The weights are the parameters in vector  $\theta$ . The neurons are gathered in layers. One or more “hidden” layers of neurons may be introduced between the input layer and the output layer. Figure 1 shows an example of a single-hidden-layer network. Each neuron of layer  $k$  receives information from the previous layer  $k - 1$ . Information from the input layer (layer 0) is propagated

to the output layer (the last layer) through the hidden layer (if any). All of the neural networks used here have a single hidden layer. The nonlinear response of a neuron to its inputs, due to the sigmoidal function, allows for the nonlinear fitting of the function parameterized by the neural network. The error introduced by the use of  $g$  instead of  $f$  depends on the distance of  $f$  to the allowed functions  $g$  on  $B$ . Given a norm  $\|\cdot\|$  on  $B$  and given  $\zeta$ , the maximum error that we tolerate, we want:

$$\exists \theta \in \mathbf{R}^p, \forall x \in A, \quad \|f(x) - g(\theta, x)\| < \zeta. \tag{2}$$

The learning phase is devoted to the optimization of the MLP. That is, according to the representativity of the learning set, the algorithm selects a vector  $\theta$  among all of the possible  $\theta$ 's. The so-called back-propagation algorithm enables us to derive the parameters in an iterative way. This method minimizes the quadratic error between the function computed by the network  $g$  and the function to be approximated  $f$  for a set of patterns for which inputs and outputs are known—the “learning set.”

**3. A neural network model for the longwave radiative transfer**

*a. Longwave radiative transfer equations*

We restrict ourselves to longwave (LW) radiative transfer modeling. The formal solution of the radiative transfer equation for a stratified cloudless atmosphere in local thermodynamic equilibrium is

$$F^\uparrow(P) = \pi \int_{-1}^{+1} \mu \, d\mu \int_\nu \, d\nu$$

$$\times \left[ I_\nu^\uparrow(P_0, \mu) \tau_\nu(P_0, P, \mu) + \int_{P_0}^P B_\nu(T_{P'}) \frac{\partial \tau_\nu(P', P, \mu)}{\partial P'} \, dP' \right] \tag{3}$$

and

$$F^\downarrow(P) = \pi \int_{-1}^{+1} \mu \, d\mu \int_\nu \, d\nu$$

$$\times \int_0^P B_\nu(T_{P'}) \frac{\partial \tau_\nu(P', P, \mu)}{\partial P'} \, dP', \tag{4}$$

where  $F^\uparrow(P)$  ( $F^\downarrow(P)$ ) is the upward (downward) radiative flux at the pressure level  $P$ , integrated over the longwave spectrum;  $I_\nu^\uparrow(P, \mu)$  is the monochromatic radiance of frequency  $\nu$  at pressure level  $P$ , propagating in a direction such that  $\mu$  is the cosine of the zenith angle;  $P_0$  is the pressure at the surface;  $\nu$  is the frequency;  $B_\nu(T_{P'})$  is the Planck function at temperature  $T_{P'}$  at pressure level  $P'$ ; and  $\tau_\nu(P', P, \mu)$  is the monochromatic flux transmittance for isotropic radiation between the levels of pressure  $P$  and  $P'$ . By introducing the



TABLE 2. Architectures of the neural networks in NeuroFlux.

	Number of neurons
(a) Clear-sky neural network	
Inputs	60
Hidden layer	30
Outputs	40
(b) Cloudy-sky neural networks	
Inputs	Between 1 and 58
Hidden layer	20
Outputs	Between 1 and 19

hidden layers are single. NN-Clr uses the 60 inputs described in the previous paragraph. The 40 outputs include 20 upward fluxes and 20 downward fluxes. The number of inputs and outputs of each one of the  $(1 + 2M)$  cloudy networks NN-Cld depends on the position of the considered cloudy layer and on the kind of flux computed. For instance, the computation of the downward flux under a black cloud that top arises at 1005 hPa uses only the temperature at 1013 hPa [see Eq. (7)]. Thus, the input number varies between 1 (computation of the downward flux under a black cloud that top arises at 1005 hPa) and 58 (computation of the upward flux above the previous black cloud). Similarly, the output number varies between 1 and 19.

Note that every neural network can compute quantities of the same form:

$$Q(P, P_b) = \int_{-1}^{+1} \mu \, d\mu \int_{\nu} d\nu \times \left[ B_{\nu}(T_{P_b}) \tau_{\nu}(P_b, P, \mu) + \int_{P_b}^P B_{\nu}(T_{P'}) \frac{\partial \tau_{\nu}(P', P, \mu)}{\partial P'} dP' \right], \quad (10)$$

where  $P$  and  $P_b$  are the pressures at the boundaries of a given atmospheric layer.

One neural network would be sufficient for the computation of all of the  $F_k^{\uparrow}$ 's and the  $F_k^{\downarrow}$ 's, both clear and cloudy, but the specialization of the neural networks in our model in selected fields of the computations improves the accuracy of the neural network simulations because it induces a smaller number of inputs and fewer parameters to set.

#### 4. Training neural networks

##### a. The TIGR (Thermodynamic Initial Guess Retrieval) dataset

It appears from the neural network method (described in section 2) that the accuracy of our scheme stems from the statistical characteristics of the training datasets of neural networks NN-Clr and NN-Clds. The essential tool for generating them is the TIGR data bank.

The second version of the data bank, TIGR-2 (Achard 1991; Escobar-Munoz 1993), groups together about 1800 atmospheric situations selected from more than 80 000 radiosonde reports collected over 10 years from all parts of the world.

The selection method is an iterative process. It relies on a distance  $D_T$ , which measures the dissimilarity in the temperature profiles of the atmospheric situations. During the first step of TIGR-2's sampling, the first atmospheric situation in the 80 000 radiosondes is archived. At step  $n$  the  $n$ th atmospheric situation is selected if its minimum distance  $D_T$  to the already archived situations is greater than an empirically chosen number  $D_T^{\min}$ . Thus, the unequal distribution of the 80 000 radiosondes over space and time disappeared. TIGR-2 can be assimilated into an almost regular networking of the observable atmospheric temperature profiles associated with their corresponding water vapor and ozone profiles.

The set is classified into quite homogeneous groups of situations determined from statistical methods, the five airmass classes: tropical (trop), midlatitude (ml1), cold temperate and summer polar (ml2), Northern Hemisphere very cold (pol1), and winter polar (pol2) (Achard 1991). TIGR-2 has been used successfully for retrieving the main thermodynamic parameters from satellite observations with a physicostatistical approach, the Improved Initialization Inversion (3I) (Chédin et al. 1985), and with neural networks [Escobar-Munoz et al. (1993), for the retrieval of temperature profiles, and Cabrera-Mercader and Staelin (1995), for the retrieval of relative humidity].

Nevertheless, two limitations in the design of the TIGR-2 dataset appeared in the framework of the present study. First, the profile selection relies only on a temperature criterion, which does not take care of the variability of the water vapor profiles. Second, the dataset does not contain enough situations with high total water vapor contents. These are mostly below  $4 \text{ g cm}^{-2}$ , whereas it has been observed that the water vapor content can exceed  $7 \text{ g cm}^{-2}$  in areas such as the warming pool in the western Pacific. These two limitations are particularly critical in the tropical class.

##### b. A new tropical class

TIGR-2's identified deficiencies mostly impact the tropical class. We undertook to reshape it. The new tropical class has been established according to the following parameters:

- the addition of atmospheric situations inferred from satellite data to the initial radiosonde dataset using the 3I algorithm and
- a new sampling method that takes the water vapor profiles into account.

The TIGR-2 dataset is based upon radiosonde reports, although they do not cover the globe equally. Instruments such as the TIROS-N (Television Infrared Ob-



by diagram of TIGR-2's tropical class. The vertical coordinate  $\Theta$  is the (liquid water) potential temperature, and the horizontal coordinate  $q$  is the water vapor mixing ratio. Each TIGR-2 tropical situation is represented by 14 points between 300 and 1013 hPa. The highest part of the profiles appears in the top left corner. For higher pressure levels, the points spread in a triangular shape, indicative of the thermodynamic constraints on the atmospheric profiles. According to their location on the diagram, a point from a situation can be attributed to a particular climatological regime: convection; radiative cooling; upper-tropospheric, meridional transport and subsidence; entrainment; and boundary layer transport (Boers and Prata 1996). Figure 3a shows an irregular spread of the points, indicating an irregular repartition of the TIGR-2 tropical situations on the climatological regimes. Figure 3b presents the same type of projection with the TIGR-3 tropical class. The overall density of the points has increased due to the increased number of atmospheric situations. More importantly, the filling is more regular. We, therefore, have improved the distribution of the different vertical climatological regimes with the new tropical class—in particular, the convection process.

#### d. Surface characteristics, CO<sub>2</sub> concentration, and cloudiness information

The learning sets that correspond to the clear and cloudy neural networks, upon which our radiative transfer scheme is based, were selected from TIGR-3. In order to take into account existing discontinuities between the surface temperature and the surface air temperature, we defined a surface temperature for each of the TIGR-3 situations with a random drawing, allowing temperature discontinuities up to 10 K. The mean long-wave surface emissivity and the CO<sub>2</sub> concentration were also randomly chosen: between 0.9 and 1.0 and between 200 and 900 ppmv, respectively. For the cloudy-sky learning datasets, black clouds in each atmospheric layer among the 19 were alternately introduced, even though the thermodynamic description of a layer sometimes made the presence of a cloud unlikely. Thus, the learning sets contain atmospheric situations that may never be observed in the atmosphere: they are not only compilations of real atmospheric situations but are also devoted to teach to the networks the computation of long-wave radiative fluxes from thermodynamic profiles. For this purpose, it is suitable that a physical phenomenon—such as the presence of a cloud in the atmospheric layers—has in the learning datasets, a regular distribution, rather than a more realistic distribution.

#### e. The vertical pressure grid

All atmospheric profiles in the learning datasets have been interpolated from the 40 pressure-level grid on which they are archived in the TIGR dataset, on the grid

that NeuroFlux uses. We defined NeuroFlux in such a way that each version of the scheme is dedicated to a specified vertical pressure grid. This is not the case with the usual wideband models, which allow the pressure grid to be changed easily. In the versions of NeuroFlux that we use in this paper, the temperature, water vapor, and ozone profiles are discretized in the middle of 19 layers, as shown in Table 1. The pressure levels of this grid are fixed. Surface pressures less than 1013 hPa can be introduced with a blackbody at the ground pressure: the altitude is treated in the same way as is cloudiness.

If one wants to choose a different vertical grid, one has to retrain the networks on this new grid. The most time-consuming computations are absorbed in the learning phase: once it is done, the method is very fast. The sigma-pressure-level grids used in most GCMs can be introduced easily by adding the surface pressure to the inputs of the scheme.

#### f. Computation of the radiative characteristics of the learning datasets

We used two radiative forward models to obtain the radiative characteristics of these profiles [the LW fluxes from (3), (4), (6), and (7)]: the ECMWF wideband operational scheme (Morcrette 1991; Zhong and Haigh 1995) and the Automatized Atmospheric Absorption Atlas line-by-line model (4A) (Scott and Chédin 1981; Tournier et al. 1995). In the following, the ECMWF wideband model will be referred to as “the WBM.” It uses averages of the absorption parameters over spectral intervals of hundreds of inverse centimeters, whereas 4A takes into account each absorption line of the different atmospheric constituents. In an earlier paper, we also presented some results of the neural network model using a narrowband model (Chéruy et al. 1996a).

The WBM refers to nine spectral intervals, for which absorption by H<sub>2</sub>O, O<sub>3</sub>, CO<sub>2</sub>, CH<sub>4</sub>, N<sub>2</sub>O, CFC-11, and CFC-12 is accounted. This model was calibrated against the Geophysical Fluid Dynamics Laboratory (Schwarzkopf and Fels 1991) line-by-line results. The parameterization of the water vapor has been improved recently by Zhong and Haigh (1995). This code is fast enough to be used in operational weather forecasts (at ECMWF) and for climate simulations (in the LMD general circulation model).

The 4A model takes into account all radiatively active atmospheric constituents, the H<sub>2</sub>O, N<sub>2</sub>, and O<sub>2</sub> continua and the CO<sub>2</sub> line coupling. This line-by-line and layer-by-layer method allows us to quickly restore monochromatic optical depths for each absorbing gas in each atmospheric layer for realistic atmospheric situations: the most time-consuming computations have been absorbed, once and for all, by precomputations, the results of which constitute the 4A atlas. The complete validation of the method for high spectral resolution is based on comparisons with the high-resolution interferometer sounder (Smith et al. 1988) measurements. The 4A mod-



TABLE 3. Mean ( $m$ ) and standard deviation ( $\sigma$ ) of 4A (line by line) and the WBM (band model) for the computation of the (a) OLR and (b) DLR for 1032 atmospheric situations. Fluxes in watts per square meter.

Model	Tropical		Midlatitude		Polar	
	$m$	$\sigma$	$m$	$\sigma$	$m$	$\sigma$
(a)						
WBM	265.5	16.4	227.7	18.9	188.4	14.5
4A	263.3	16.4	226.1	18.8	187.7	14.6
WBM-4A	2.1	0.7	1.6	0.7	0.7	1.1
(b)						
WBM	314.9	48.6	221.7	34.7	155.5	19.9
4A	312.5	47.4	222.9	33.0	158.7	19.7
WBM-4A	2.4	2.0	-1.3	1.9	-3.3	0.8

between the cooling rates from 4A and from WBM reaches  $0.4 \text{ K day}^{-1}$  at 300 hPa and near the ground in the tropical class (Fig. 4). The sign changes around 500 hPa. Compared with 4A, the WBM tends to cool the high troposphere and heat the boundary layer. The standard deviations are of the order of  $0.2 \text{ K day}^{-1}$  above 600 hPa and increase below. Overall, the differences increase with the water vapor content. For the OLR, the mean difference is between  $2.1 \text{ W m}^{-2}$  in the tropical class and  $0.7 \text{ W m}^{-2}$  in the polar class. The standard deviations are about  $0.7 \text{ W m}^{-2}$ . For the DLR, the differences are larger, with an rms of the order of  $3 \text{ W m}^{-2}$ .

## 5. Performances

### a. NeuroFlux-A: Comparisons with WBM using radiosonde data

The  $F_n^{\uparrow}$ 's and the  $F_n^{\downarrow}$ 's for the training of the neural networks were first computed with WBM. These learning datasets led to a first version of our neural network model, called NeuroFlux-A.

Radiative fluxes obtained by using either NeuroFlux-A or WBM have been compared for the 1032 radiosonde reports from the set S. None of them was used in the learning datasets of the neural networks. For the three air mass classes, we computed the biases and standard deviations of the differences between the radiative calculations of NeuroFlux-A and WBM. The computations are performed cloudless. Results are shown in Fig. 5. The standard deviations are about  $0.2 \text{ K day}^{-1}$ . The absolute value of the biases are less than  $0.05 \text{ K day}^{-1}$  in the midlatitude and polar classes. In the tropical class the absolute value is slightly higher but less than  $0.1 \text{ K day}^{-1}$  except near the ground, where the bias reaches  $-0.2 \text{ K day}^{-1}$ . Compared with Fig. 4, the standard deviations are similar, but the biases are significantly smaller. Because NeuroFlux is based on principles that differ greatly with the principles of WBM, the maximum errors are also interesting characteristics of the validation. For NeuroFlux-A, the maximum error in the troposphere equals  $1.8 \text{ K day}^{-1}$ , less than the maximum error of the WBM compared with 4A, which reaches  $2.9 \text{ K day}^{-1}$ .

For the computation of OLR and DLR (Table 4), the standard deviations are similar to those between WBM and 4A:  $1.0 \text{ W m}^{-2}$  for OLR and  $1.6 \text{ W m}^{-2}$  for DLR. The biases, whose absolute value is less than  $1.0 \text{ W m}^{-2}$ , are significantly smaller.

We checked the accuracy of the cloudy neural networks by artificially adding black clouds in the radiosondes and comparing the corresponding computations of the WBM and NeuroFlux-A. The neural network-based model exhibits, with WBM, differences similar to the ones observed in clear-sky situations (results not shown).

### b. NeuroFlux-A: Comparisons with the WBM using TOVS 3I global data

To study the robustness of the method, we have extended the previous comparisons between the two models, WBM and NeuroFlux-A, to an observation dataset consisting of two years of global data. To do so, we used the geophysical parameters inferred from TOVS data, actually the TOVS 3I-retrieved products morning path, obtained from April 1987 to March 1989 (Scott et al. 1996). The computation of the radiative fluxes from the TOVS 3I products using WBM is explained in Chéruy et al. (1996b). Each month groups together hundreds of thousands of tropical, midlatitude, and polar clear and cloudy atmospheric situations. We computed the global monthly mean error of the instantaneous differences. For upward flux calculations (Fig. 6a), the rms of differences between NeuroFlux-A and WBM remains between 1 and  $2 \text{ W m}^{-2}$ , which represents less than 0.6% of the upward flux values. For downward fluxes (Fig. 6b), the results are similar with a larger difference around 500 hPa of about 4%. This larger error is due to both a particularity in the TOVS 3I-retrieved profiles and the way NeuroFlux parameters are inferred. The water vapor profiles inferred from TOVS 3I—actually amounts in four coarse layers—sometimes present important discontinuities at 500 hPa. Now, in their computations, the neural networks exploit the correlations that usually exist in the learning datasets between successive water vapor specific humidities in the water va-



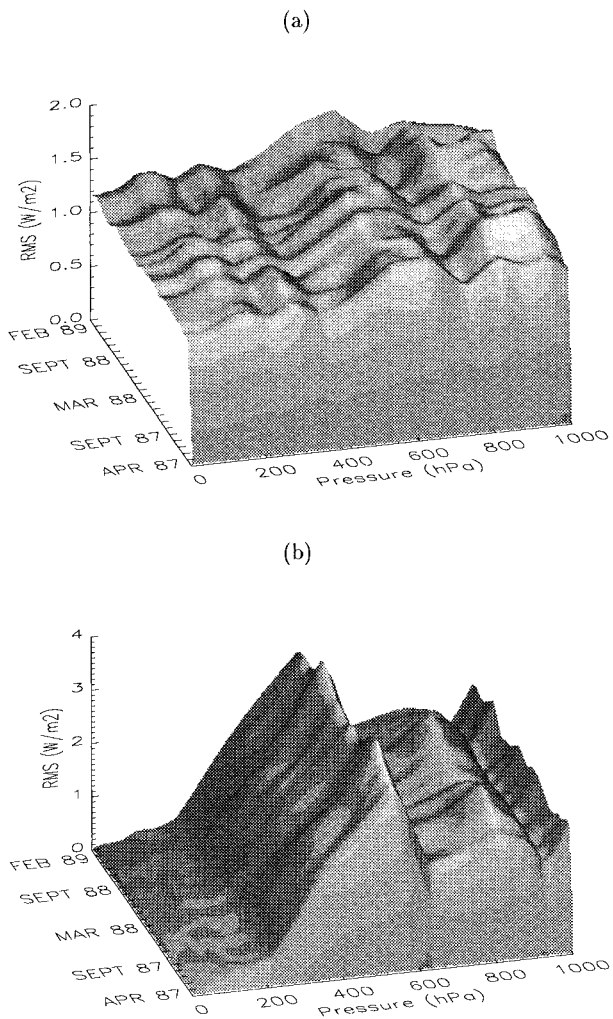


FIG. 6. Evolution of the rms of the differences between NeuroFlux-A and WBM for the computation of (a) upward fluxes and (b) downward fluxes during two years of global data ( $\text{W m}^{-2}$ ). Values are given on a 20 pressure-level grid.

1988, although these two months were used for the extension of TIGR-2. The stability of the method enables us to use the code for long-term and global simulations, as is done in numerical models of atmospheric circulation.

#### c. NeuroFlux-B: Comparisons with 4A

For NeuroFlux-B, the longwave fluxes of the learning datasets for the neural networks are computed with 4A. We carried out the validation of the parameterization on the 1032 radiosonde reports from the set S. Figure 7 shows the results for the computation of the cooling rates, and Table 5 shows the results for the computation of the OLR and DLR in clear situations. Although the training model is much more accurate, the differences between NeuroFlux-B and 4A are similar to the ones between NeuroFlux-A and WBM. Compared to the ones

between WBM and 4A, the standard deviations are similar, but the biases are significantly smaller. The validation of the NeuroFlux-B cloudy-skies neural networks gave similar results (not shown).

Therefore, the neural network parameterization using line-by-line computations appears to be more accurate than the classic parameterization of WBM.

#### d. NeuroFlux-B: Doubling $\text{CO}_2$ concentrations experiment

The computing time of NeuroFlux-B reference code (4A) forbids global long-term validations of NeuroFlux-B as was done with NeuroFlux-A, though other kinds of validations are possible: in particular, the classic sensitivity study doubling concentrations of  $\text{CO}_2$ . Indeed, for a climate model it is particularly important to obtain the correct tendency to changes in  $\text{CO}_2$  concentrations. To assess this sensitivity, both 4A and NeuroFlux-B were used to compute the differences in cooling rates for set S resulting from doubling concentrations of  $\text{CO}_2$  from its current level of 355 to 710 ppmv. For brevity, only the results for the tropical class are shown. Figure 8a presents the mean and standard deviation of the 4A computations. They show known features of the atmospheric response to increased  $\text{CO}_2$  (e.g., Schlesinger and Mitchell 1987): the stratosphere cools and the troposphere warms. Figure 8b presents NeuroFlux-B computations and the corresponding error. NeuroFlux-B reproduces the stratospheric tendency well with negligible biases and standard deviations. In the troposphere, where the change in cooling rate is far smaller, the error is characterized by a standard deviation of about  $0.03 \text{ K day}^{-1}$ , that is, more than half of the rms signal (about  $0.05 \text{ K day}^{-1}$ ). Nevertheless, the error bias is less than  $0.01 \text{ K day}^{-1}$  when the mean signal is about  $0.04 \text{ K day}^{-1}$ .

Every parameterization method brings noise into the realizations of a function  $f$  to be computed. The results of NeuroFlux-B validation show that the noise introduced by the neural networks is small for computations of individual fluxes or cooling rates but is not negligible in sensitivity tests, though the mean tendency is well reproduced by the method. This is very fundamental for climate studies.

#### e. Computing time

The architecture of the neural networks enables fast computations with modern computers in spite of the number of parameters the neural networks include. We compared the computing times of NeuroFlux-A and NeuroFlux-B to the computing times of WBM and 4A, respectively.

The computing times of our schemes vary according to the number of cloud layers since for each additional layer in the atmosphere the algorithm includes two more neural networks to perform the computations. Figure 9





## REFERENCES

- Achard, V., 1991: Trois problèmes clés de l'analyse 3D de la structure thermodynamique de l'atmosphère par satellite: Mesure du contenu en ozone; classification des masses d'air; modélisation hyper rapide du transfert radiatif. Ph.D. thesis, Université Paris VI, 168 pp. [Available from LMD, Ecole Polytechnique, 91128 Palaiseau Cedex, France.]
- Boers, R., and J. Prata, 1996: Thermodynamic structure of the maritime troposphere around the Australian continent. *Int. J. Climate*, **16**, 1–18.
- Cabrera-Mercader, C. R., and D. H. Staelin, 1995: Passive microwave relative humidity retrievals using feedforward neural networks. *IEEE Trans. Sci. Remote Sens.*, **33**, 1324–1326.
- Cess, R. D., and Coauthors, 1993: Uncertainties in carbon dioxide radiative forcing in atmospheric general circulation models. *Science*, **262**, 1252–1255.
- Chédin, A., N. A. Scott, C. Wahiche, and P. Moulinier, 1985: The Improved Initialization Inversion method: A high-resolution physical method for temperature retrievals from satellites of the TIROS-N series. *J. Climate Appl. Meteor.*, **24**, 128–143.
- Chéruy, F., F. Chevallier, J.-J. Morcrette, N. A. Scott, and A. Chédin, 1996a: A fast method using neural networks for computing the vertical distribution of the thermal component of the Earth radiative budget (in French). *C. R. Acad. Sci. Paris*, **322** (IIb), 665–672.
- , —, N. A. Scott, and A. Chédin, 1996b: Use of the vertical sounding in the infrared for the retrieval and the analysis of the longwave radiative budget. *IRS '96: Current Problems in Atmospheric Radiation*, W. L. Smith and K. Stamnes, Eds., A. Deepak, 375–376.
- Chevallier, F., 1998: La modélisation du transfert radiatif à des fins climatiques: Une nouvelle approche fondée sur les réseaux de neurones artificiels. Ph.D. thesis, University Paris VII, 225 pp. [Available from LMD, Ecole Polytechnique, 91128 Palaiseau Cedex, France.]
- Ellingson, R. G., and J. Ellis, 1991: The intercomparison of radiation codes used in climate models: Longwave results. *J. Geophys. Res.*, **96** (D5), 8929–8953.
- Escobar-Munoz, J., 1993: Base de données pour la restitution de variables atmosphériques à l'échelle globale. Étude sur l'inversion par réseaux de neurones des données des sondes verticales atmosphériques satellitaires présents et à venir. Ph.D. thesis, Université Paris VII, 190 pp. [Available from LMD, Ecole Polytechnique, 91128 Palaiseau Cedex, France.]
- , A. Chédin, F. Chéruy, and N. A. Scott, 1993: Réseaux de neurones multi-couches pour la restitution de variables thermodynamiques atmosphériques à l'aide de sondes verticales satellitaires. *C. R. Acad. Sci. Paris*, **317** (IIb), 911–918.
- Harshvardhan, D. A. Randall, and T. G. Corsetti, 1987: A fast radiation parameterization for atmospheric circulation models. *J. Geophys. Res.*, **92**, 1009–1016.
- Morcrette, J.-J., 1991: Radiation and cloud radiative properties in the European Centre for Medium-Range Weather Forecasts forecasting system. *J. Geophys. Res.*, **96** (D5), 9121–9132.
- Moulinier, P., 1983: Analyse statistique d'un vaste échantillonnage de situations atmosphériques sur l'ensemble du globe. LMD Internal Note 123, 30 pp. [Available from LMD, Ecole Polytechnique, 91128 Palaiseau Cedex, France.]
- Rumelhart, D. E., G. E. Hinton, and R. J. Williams, 1986: Learning internal representations by error propagation. *Parallel Distributed Processing: Explorations in the Macrostructure of Cognition 1*, D. E. Rumelhart and McClelland, Eds., MIT Press, 318–362.
- Sadourny, R., and K. Laval, 1984: January and July performances of the LMD general circulation model. *New Perspectives in Climate Modelling*, A. L. Berger and C. Nicolis, Eds., Elsevier, 173–198.
- Schlesinger, M. E., and J. F. B. Mitchell, 1987: Climate model simulations of the equilibrium climatic response to increased carbon dioxide. *Rev. Geophys.*, **25**, 760–798.
- Schwarzkopf, M. D., and S. B. Fels, 1991: The simplified exchange method revisited: An accurate, rapid method for computation of infrared cooling rates and fluxes. *J. Geophys. Res.*, **96** (D5), 9075–9096.
- Scott, N. A., and A. Chédin, 1981: A fast line-by-line method for atmospheric absorption computations: The Automated Atmospheric Absorption Atlas. *J. Appl. Meteor.*, **20**, 802–812.
- , and Coauthors, 1996: Re-analysis of a multi-year archive of TOVS/ NOAA satellite data for climate studies. *Proc. Global Energy and Water Cycle Symp.*, Washington, DC, World Meteorological Organization, 375–376.
- Smith, W. L., H. M. Woolf, H. B. Howell, H. L. Huang, and H. E. Revercomb, 1988: The simultaneous retrieval of atmospheric temperature and water vapor profiles—Applications to measurements with the high spectral resolution infrared sounder (HIS). *RSRM '87: Advances in Remote Sensing Retrieval Methods*, A. Deepak, H. Fleming, and J. S. Theon, Eds., A. Deepak, 189–202.
- Stephens, G. L., 1978: Radiation profiles in extended water clouds. II: Parameterization schemes. *J. Atmos. Sci.*, **35**, 2123–2132.
- , D. L. Jackson, and I. Wittmeyer, 1996: Global observations of upper-tropospheric water vapor derived from TOVS radiance data. *J. Climate*, **9**, 305–325.
- Tournier, B., R. Armante, and N. A. Scott, 1995: Stransac-93, 4A-93. Développement et validation des nouvelles versions des codes de transfert radiatif pour application au projet IASI. LMD Internal Note 201, 43 pp., [Available from LMD, Ecole Polytechnique, 91128 Palaiseau Cedex, France.]
- Wilson, C. A., and J. F. B. Mitchell, 1986: Diurnal variation and cloud in General Circulation Model. *Quart. J. Roy. Meteor. Soc.*, **112**, 347–369.
- Zhong, W., and J. D. Haigh, 1995: Improved broadband emissivity parameterization for water vapor cooling rate calculations. *J. Atmos. Sci.*, **52**, 124–138.